Biophysical Journal Volume 108 April 2015 1878–1886

Article

Model for Probing Membrane-Cortex Adhesion by Micropipette Aspiration and Fluctuation Spectroscopy

Ricard Alert,[1] Jaume Casademunt,[1] Jan Brugués,[2,*] and Pierre Sens[3,*]

[1]Departament d'Estructura i Constituents de la Matèria, Universitat de Barcelona, Barcelona, Spain; [2]Max Planck Institute of Molecular Cell Biology and Genetics, Max Planck Institute for Physics of Complex Systems, Dresden, Germany; and [3]Laboratoire Gulliver, Centre National de la Recherche Scientifique-ESPCI Paris Tech, UMR 7083, Paris, France

ABSTRACT We propose a model for membrane-cortex adhesion that couples membrane deformations, hydrodynamics, and kinetics of membrane-cortex ligands. In its simplest form, the model gives explicit predictions for the critical pressure for membrane detachment and for the value of adhesion energy. We show that these quantities exhibit a significant dependence on the active acto-myosin stresses. The model provides a simple framework to access quantitative information on cortical activity by means of micropipette experiments. We also extend the model to incorporate fluctuations and show that detailed information on the stability of membrane-cortex coupling can be obtained by a combination of micropipette aspiration and fluctuation spectroscopy measurements.

INTRODUCTION

In many cells, a thin layer of cytoskeleton called "cortex" underlies the plasma membrane. While the cellular membrane serves as a barrier for the cell and a mechanism to communicate with the extracellular media, the cortex, made mostly of actin cross-linked filaments and myosin II, provides rigidity and allows for active remodeling of the cell boundaries, essential for instance for cell motility. The control of membrane-cortex adhesion is crucial to many cellular processes. Indeed, membrane-cortex detachment and the formation of cellular blebs, spherical protrusions of the unbound plasma membrane, is often a sign of apoptosis (1,2). Membrane blebbing is also used for motility by several cell types, including amoebae and possibly cancer cells (3–6).

It is acknowledged that membrane-cortex adhesion is obtained via specific interactions between large numbers of ligand and receptor molecules (7), such as Talin (8) and ezrin/radixin/moesin proteins (9). Spontaneous membrane detachment, also known as blebbing, has been associated with myosin activity within the cortex (10,11). Externally induced perturbations using micropipette aspiration or osmotic shocks show that a sufficiently large drop of external pressure can induce membrane detachment (12). Consequently the links between the membrane and cortex are constantly under stress, which origin is ultimately related to acto-myosin cortical tension and osmotic pressure.

In this article, we present a model for adhesion based on the kinetics of the membrane-cortex ligands (13–16). We describe the stability of adhesion by coupling the kinetics of the ligands to the stress exerted on them and to physical properties of the membrane. In its simplest form, the model establishes the mechanical equilibrium of the cell considering both the pressure drop across the membrane and the prestressed state of the cortex, and predicts the outcome of a micropipette aspiration experiment in terms of physical parameters. These predictions are then compared to experiments from the literature. We also discuss extensions of the model to include spatial modulations of the membrane and different scenarios of hydrodynamic interactions, depending on the porosity of the cortex and its actual distance to the membrane. In particular, we obtain analytical expressions for the structure factor and fluctuation spectrum of the membrane in certain limits, and show how these results may be used to obtain additional information on the density of ligands by means of fluctuation spectroscopy experiments on eukaryotic cells.

MATERIALS AND METHODS

The adhesion of a flexible membrane on a substrate by means of discrete linkers has been extensively studied in the past (18–23), mostly using computer simulations. It is a highly nontrivial problem due to the multiplicity of energy scales (membrane rigidity and tension, linker stiffness, and binding energy) and timescales (membrane and cytosol fluidity, linker's diffusion, and binding kinetics). In particular, the role of fluctuations on the unbinding transition of a membrane possessing metastable bound and unbound states has been characterized numerically (19), but the unbinding of a membrane subjected to a constant pressure has, to our knowledge, not been systematically investigated. Our primary goal here is to assess the role of cortical prestress on membrane-cortex detachment.

To this aim, we first adopt a highly simplified model, where we assume a nearly planar membrane subject to a normal external stress σ and attached to the cortex by a density of linkers ρ_b, which is necessarily smaller than a

Submitted August 6, 2014, and accepted for publication February 25, 2015.

*Correspondence: brugues@mpi-cbg.de or pierre.sens@curie.fr

Pierre Sens's present address is Physico-Chimie Curie, CNRS UMR 168, Institut Curie, 11 rue Pierre et Maris Curie, Paris, France.

Editor: Cecile Sykes.

0006-3495/15/04/1878/9 $2.00

http://dx.doi.org/10.1016/j.bpj.2015.02.027

maximal value ρ_0 (Fig. 1). The cortex is assumed to be flat and immobile, so that the model is only valid at length scales below the correlation length for cortex undulations. For a constant normal stress σ, an equilibrium state may exist with a planar membrane at position u where a uniform density ρ_b of bound springlike linkers with elastic constant k balances the external force. To find the conditions for the existence and stability of such an equilibrium state, we may write dynamical equations assuming spatial uniformity, where u and ρ_b are only time-dependent,

$$\eta\frac{du}{dt} = \sigma - ku\rho_b, \tag{1}$$

$$\frac{d\rho_b}{dt} = k_{\rm on}[\rho_0 - \rho_b] - k_{\rm off}(u)\rho_b, \tag{2}$$

where η is an effective viscosity per unit length, and $u = 0$ corresponds to the position for which the bound linkers are not stretched. For small membrane displacements, the relevant contribution to dissipation is due to cytosol flow through the cortex meshwork, and the effective parameter η can be estimated as $\eta \sim \eta_c h/\xi^2$ (see Section S1 in the Supporting Material for details), where $\xi \sim 30$ nm is the scale of the cortex mesh size (24), $h \sim 500$ nm is the thickness of the cortex, and $\eta \sim 3\times10^{-3} - 2\times10^{-1}$ Pa s is the cytosol viscosity (10).

The linker kinetics is defined by the attachment and detachment rates $k_{\rm on}$ and $k_{\rm off}$ (Fig. 1), and is assumed to be much faster than the typical timescale of membrane shape relaxation. The force-dependent kinetics of the linkers then imposes a strong nonlinear coupling between the kinetics and the position of the membrane. The detachment rate is assumed to follow a Kramer's-like kinetics (25) appropriate to thermally induced processes,

$$k_{\rm off}(u) = k_{\rm off}^0 e^{ku\delta/(k_{\rm B}T)}, \tag{3}$$

where δ is a characteristic bond length in the nanometric scale (17). For simplicity, we assume linker attachment to be an active process occurring at a constant rate $k_{\rm on}$. Therefore, detailed balance is not obeyed, as previously considered in membrane adhesion problems (18). This assumption allows us to disregard membrane fluctuations between attachment points, and yields a simple analytical form for the unbinding transition. However, it does not capture binding cooperativity occurring due to the smoothing of membrane fluctuations near attachment points (19–23).

Two relevant dimensionless quantities characterize the mechanics of the linkers: the kinetic ratio, χ, and the ratio of the force on the membrane to an intrinsic force scale of the linkers, α, with

$$\chi \equiv \frac{k_{\rm off}^0}{k_{\rm on}} \quad \text{and} \quad \alpha \equiv \frac{\sigma\delta}{\rho_0 k_{\rm B}T}. \tag{4}$$

Equilibrium solutions to Eqs. 1 and 2 exist only for $\alpha < \alpha^*$, where the latter is defined by

$$\alpha^* e^{1+\alpha^*} = \chi^{-1}. \tag{5}$$

Taking $\chi \sim 10^{-3}$ (26) and $\delta \sim 1$ nm, the critical force per link is $\sigma^*/\rho_0 \sim 18$ pN, corresponding to ~4.5 times the thermal force per link $k_{\rm B}T/\delta$. This fixes the condition for the detachment of the membrane from the cortex, which occurs for stresses that surpass the critical stress $\sigma^* = \rho_0\alpha^*(\chi)k_{\rm B}T/\delta$.

The adhesion energy w per unit area may be defined as the work necessary to bring the stress of the linkers from its rest value to the critical value for detachment in a quasi-static fashion, that is,

$$w(u_{\rm eq}) = \int_{u_{\rm eq}}^{u^*}\sigma(u)du = \rho_0 k\int_{u_{\rm eq}}^{u^*}\frac{u}{1+\chi e^{ku\delta/(k_{\rm B}T)}}du, \tag{6}$$

where $\sigma(u)$ is the equilibrium stress for each u. Note that the adhesion energy depends on the actual state of the cell $u_{\rm eq}$, which is generically unknown and incorporates the prestress state of the cell due to cortical tension.

Within our simplified model, the average density of bound linkers $\rho_{b,\rm eq}$, the critical stress σ^*, and the adhesion energy w all scale linearly with the density of available linkers ρ_0. This scaling results from our assumption of a constant binding rate. A different scaling is expected if the binding rate depends on the average position and fluctuations of the free membrane between anchoring points. If the on-rate obeys detailed balance, one expects $\rho_{b,\rm eq} \sim \rho_0^2$ in the absence of a pressure difference (20,21). As discussed in the following sections, the results of micropipette experiments are consistent with a linear scaling $\sigma^* \sim \rho_0$.

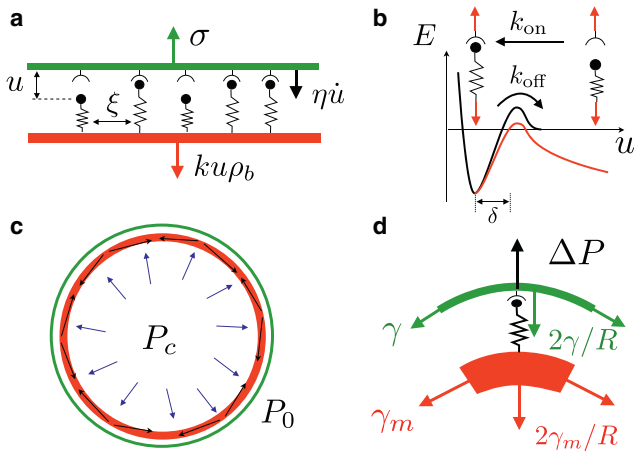

FIGURE 1 Sketch of the system. (*a*) The ligands are modeled as springs that link the cortex (*red*) and the membrane (*green*). (*b*) Kinetic rates $k_{\rm on}$ and $k_{\rm off}$ of the ligands. The value $k_{\rm off}$ depends on the load (17). (*c*) Forces involved in the cell at steady state: internal pressure, P_c, and external pressure, P_0, exert a normal force on the membrane and cortex, which is compensated by the membrane and cortex tension. (*d*) The normal projection of the acto-myosin tension in the cortex is transmitted to the membrane through proteins that link the cortex and the membrane. To see this figure in color, go online.

RESULTS AND DISCUSSION

The simplified stochastic model of adhesion outlined in the previous section is used below to analyze two different kinds of experiments that can probe membrane-cortex interaction. First, we analyze micropipette experiments where the critical suction pressure required to unbind the cell membrane from the cortex was measured in different cellular contexts, where the density of adhesion molecules and of cortical motors have been altered. Second, we derive the effect of membrane-cortex interaction on the membrane fluctuation spectrum. There is as of yet no experimental data that can be directly confronted to the latter derivation. We hope this article will foster experimental spectroscopy studies that will couple membrane fluctuation analysis with cell micromanipulation, along the lines described below.

Mechanical equilibrium of the cell

Force balance at the membrane involves the difference of pressure across the membrane, ΔP, and the normal projection of the cortex and membrane tension, γ_m and γ, respectively,

$$\Delta P = (\gamma_m + \gamma)\frac{2}{R},$$

where R is the radius of the cell, assumed spherical. At equilibrium, the links sustain the stress needed to maintain the cortex and the membrane adhered, $\sigma_{eq} = 2\gamma_m/R$, which accounts for the difference between the pressure and the membrane tension stresses, $\Delta P - 2\gamma/R$. Whenever the equilibrium stress exceeds the critical value σ^*, we expect the cell membrane to detach spontaneously.

Micropipette aspiration (12,16,27–29), among other techniques (11,30,31), allows us to apply pressure perturbations of controlled intensity and area. Pressure perturbations can be supplemented with perturbations on relevant cell parameters such as myosin activity and link or cortex density, by genetics (27–29) or direct drug treatment (10,11,31). Tether pulling experiments have also been used to probe membrane-cortex adhesion (32), but their interpretation is rather nontrivial (33). In the following, we restrict ourselves to a quantitative interpretation of micropipette aspiration experiments.

Micropipette aspiration

During a micropipette experiment, a pressure drop is applied on a small region of the membrane defined by the micropipette radius R_p. A new equilibrium state in the micropipette requires an increase of the stress exerted on the links with respect to σ_{eq},

$$\sigma = \Delta P_p - 2\gamma\left(\frac{1}{R_p} - \frac{1}{R}\right) + 2\frac{\gamma_m}{R}, \qquad (7)$$

where $\Delta P \equiv P_0 - P_p$ is the difference between the extracellular media and the aspiration pressure, and R is the radius of the cell after deformation. Characteristic bounds for membrane tension $\gamma \lesssim 10^{-4}$ N/m and radius of cell $R \sim 10$ μm and pipette $R_p \sim 5$ μm allow membrane tension to compensate for a pressure of ~20 Pa, which is small compared to the range of experimental pressures ~100–1000 Pa. As a consequence, we will neglect the membrane tension contribution in the following. The last term in the right-hand side accounts for the cortical stress, or prestressed state of the cell σ_{eq}. In general, force balance does not need to be satisfied and the cell will eventually be entirely sucked inside the pipette if the suction pressure ΔP_p is too large (16). Here we focus on the case where the cortex is able in principle to compensate for the pipette pressure.

Using our previous analysis for the membrane-cortex adhesion, we can relate the critical stress for the links, σ^*, with the critical aspiration pressure needed to unbind the membrane via Eq. 7:

$$\Delta P_p^* = \rho_0 \alpha^* \frac{k_B T}{\delta} - 2\frac{\gamma_m}{R}. \qquad (8)$$

The critical aspiration pressure has two contributions: the pressure needed to detach a certain number of relaxed links, given by the density of ligands and the critical force per link (first term); and the contribution from the presence of actomyosin tension in the cortex, which sets a nonzero stress on the links at equilibrium, hence reducing the amount of pressure needed to reach the critical stress (second term, Fig. 2 *a*).

As in determining the critical aspiration pressure, we find that the adhesion energy per unit area measured when detaching the membrane (Eq. 6) depends on the level of

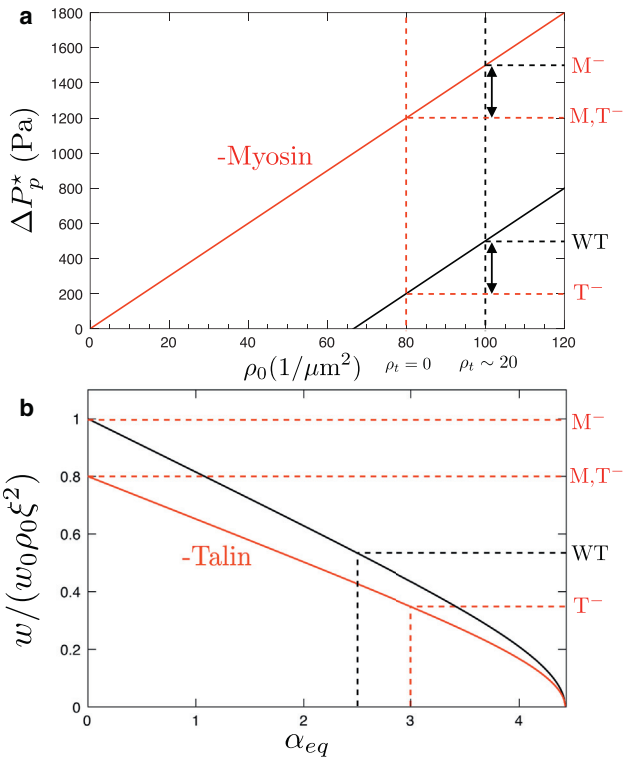

FIGURE 2 Theoretical predictions for the critical aspiration pressure and adhesion energy in a micropipette experiment. (*a*) Critical pressure as a function of the density of linkers ρ_0 according to Eq. 8. (*Solid black* and *red lines*) Cells with and without myosin II, respectively. (*Horizontal dashed lines*) Experimentally measured value of the critical detachment pressure (28) for wild-type cells (*WT*), mutants lacking myosin (M^-), mutants lacking talin (T^-), and double mutants (M, T^-). The slope and height of the two theoretical curves is entirely determined by these critical pressures (see text). (*b*) Effective adhesion energy as a function of the equilibrium cortical tension in the cell according to Eq. 9. (*Solid black* and *red lines*) Cells with and without talin, respectively. To see this figure in color, go online.

cortical rest tension, $\sigma_{eq} = 2\gamma_m/R$, which ultimately determines the effective number of ligands to be broken:

$$w = w_0\overline{\rho}_0 \int_{z_{eq}}^{z^*} \frac{z}{1+\chi e^z} dz. \quad (9)$$

Here, $w_0 \equiv (k_BT/\delta)^2/(k\xi^2)$ is an upper bound for the adhesion energy, that corresponds to nonprestressed ligands, and for clarity we have used rescaled quantities for the stretching, $z \equiv u/u_0$ with $u_0 \equiv k_BT/(k\delta)$, and ligand density $\overline{\rho}_0 \equiv \rho_0\xi^2$. The adhesion energy per unit area depends linearly on the saturation density of links, $w \sim w_0\overline{\rho}_0$, but contains a correction factor that includes the prestressed state of the cell. In the presence of cortical tension in the cell, there is both a reduction of the number of effective bound links, and an increase of stress per link. Consequently, close to the unbinding transition, the adhesion energy is reduced in a strongly nonlinear way by increasing the cortex prestress (Fig. 2 *b*).

Discussion of micropipette experiments

Our model allows us to directly relate the critical perturbation pressure needed to detach the membrane from the cortex to two physiologically relevant quantities: the density of membrane-cortex ligands, and the myosin-driven cortical tension (Eq. 8). This relationship provides not only a rational explanation for the membrane unbinding for a variety of cell phenotypes where either the density of ligands or myosin activity is altered, but also a method to directly probe cortex activity by measuring the critical pressure needed to unbind the membrane.

We refer to previous experimental results concerning the abrupt unbinding induced by micropipette suction to assess the validity of our model (12,28). To test the relationship among critical pressure, ligand density, and cortical tension, we would ideally need to measure the critical pressure for cells whose phenotype has been quantitatively altered. Merkel et al. (28) considered four phenotypes of the amoebae *Dictyostelium*: wild-type, myosin-inhibited, talin-inhibited (a membrane-cortex linker), and double mutants. These four phenotypes are sufficient to qualitatively test our model and obtain values for all the relevant parameters.

Mutations that perturbed ligand density and cortex activity should be independent within our model. Accordingly, the difference of unbinding pressure for two values of ligand density must be the same independently of the value of cortical activity (Fig. 2 *a*). In Merkel et al. (28), the decrease of critical pressure between the wild-type and talin-inhibited amoebae is comparable to the corresponding decrease between the myosin-inhibited and double-inhibited mutants (~150–200 Pa and ~150–500 Pa, respectively), even though the actual values of the cortical tension with and without myosin differ by a factor of 5 due to cortical prestress. This suggests that the critical pressure scales linearly with the density of available bounds: $\Delta P_p^* \sim \rho_0$, as predicted by our simple model (Eq. 8). Comparing the critical pressures in both wild-type and myosin-null cells for a fixed link density (Figs. 3b and 4b in Merkel et al. (28)), we can estimate the myosin-driven cortical stress in the wild-type amoeba,

$$\gamma_m = \left(\Delta P_p^{*M^-} - \Delta P_p^*\right)\frac{R}{2} \sim 5 \times 10^{-3}\text{N/m}.$$

This is at least two orders-of-magnitude higher than the typical membrane tension of a vesicle, γ, and contributes to the 60% of the ~1600 Pa needed to unbind the membrane. This estimate of the cortical tension agrees well with direct experimental measurements in *Dictyostelium* (27). Finally, introducing the obtained value of γ_m into the rest stress $\sigma_{eq} = 2\gamma_m/R$, and using the stationary state solution of Eqs. 1 and 2, $z_{eq} = \alpha_{eq}(1+\chi e^{z_{eq}})$, the equilibrium stretching of the linkers can be found, $u_{eq} \sim 100$ nm, as well as that roughly all the linkers are connected in equilibrium conditions for the wild-type cells, $\rho_{b,eq}/\rho_0 = \alpha_{eq}/z_{eq} \sim 1$.

For myosin-inhibited amoebae, the micropipette pressure is directly related to the available density of links (Eq. 8). Using the results from Merkel et al. (28), we can estimate the relative concentration of talin with respect to the saturation link concentration:

$$\frac{\rho_t}{\rho_0} = \frac{\Delta P_p^{*M^-} - \Delta P_p^{*M,T^-}}{\Delta P_p^{*M^-}} \sim 10 - 30\%.$$

Assuming the saturation density to be $\rho_0 \sim 100$ links/μm^2, talin density should be roughly $\rho_t \sim 20$ links/μm^2. The asymmetric distribution of this small density of talin links seems to be enough to drive directed motion in amoebae (28). Similar observations are reported for zebrafish cells (31). For completeness, assuming a ligand length $\delta \sim 1$ nm, we find

$$\alpha^* = \frac{\Delta P_p^{*M^-}\delta}{\rho_0 k_BT} \sim 4,$$

and the critical force per link $\sigma^*/\rho_0 \sim 16$ pN is four times the thermal force of the link k_BT/δ, which is close to our initial estimate (~18 pN). This quantity is independent of the cell phenotype and only depends on the kinetic rate ratio χ. In fact, from the experimental estimate of α^*, we can derive the kinetic ratio of on- and off-rates of the membrane-cortex linkers, $\chi \sim 10^{-3}$, in agreement with Rognoni et al. (26). Moreover, using the stationary solution of our model, a critical stretching $u^* \sim 200$ nm and a critical fraction of bound linkers $\rho_b^*/\rho_0 \sim 0.9$ are found. Our results show that the rest stress $\sigma_{eq} = 2\gamma_m/R$ is ~60% of the critical unbinding value σ^* for wild-type cells, while it is ~75% in talin-null cells. This is consistent with the observation that spontaneous blebbing of migratory *Dictyostelium* is more frequent for talin-null mutants than for wild-type cells (34).

Finally, our model gives a prediction for the adhesion energy as a function of the ligand density and cortical activity

(Eq. 9). In the case of the four phenotypes discussed above, the maximum adhesion energy is $w_0\rho_0\xi^2 \sim 2 \times 10^{-5}$ J/m^2, and corresponds to the mutant lacking myosin (a nonprestressed cell, $\alpha_{\rm eq} = 0$). For a mutant lacking Talin and myosin II, the adhesion energy is reduced by ~10–30% due to the decrease in ρ_0. For a wild-type cell and a mutant lacking talin, the adhesion energies are further reduced, by 50% and 65%, respectively, due to cortical prestress (Fig. 2 *b*). The dramatic increase in the adhesion energy for a cell lacking myosin activity, which can be ~200%, illustrates the importance of cortex activity in the cell in determining the experimental measurements of adhesion energy and detachment pressures. Table 1 recapitulates the numerical values used for the parameters of the model. These parameters may vary significantly depending on cell lines and experimental conditions, so this choice is somewhat arbitrary. However, we emphasize that both the cortical tension γ_m and the fraction of bonds associated with Talin ρ_t/ρ_0 do not depend on this choice and can be directly determined by confronting Eq. 8 with the experimental results.

Membrane undulations

The model for membrane-cortex adhesion discussed so far considers a flat membrane, disregarding possible membrane undulations. In this section, we address the linear dynamics of long-wavelength perturbations around the flat membrane state:

$$\begin{aligned} u(\vec{x},t) &= u_{\rm eq} + \delta u(\vec{x},t), \\ \rho_b(\vec{x},t) &= \rho_{b,\rm eq} + \delta\rho_b(\vec{x},t). \end{aligned} \tag{10}$$

The coarse-grained interface Hamiltonian includes the elastic energy of bound linkers and contributions from the membrane bending rigidity and tension (35),

$$\begin{aligned} \mathcal{H} = \int_S \Big[&\frac{\kappa}{2}\left[\nabla^2 u(\vec{x})\right]^2 + \frac{\gamma}{2}\left[\vec{\nabla} u(\vec{x})\right]^2 \\ &+ \frac{k}{2}\rho_b(\vec{x})u^2(\vec{x}) - \sigma u(\vec{x})\Big] d^2\vec{x}, \end{aligned} \tag{11}$$

TABLE 1 Estimates for model parameters

Symbol	Description	Estimate (Ref.)
ξ	cortex mesh size	30 nm (24)
h	cortex thickness	500 nm (10)
η_c	cytosol viscosity	10^{-2} Pa s (10)
$k_{\rm on}$	linker attachment rate	10^4 s^{-1} (26)
$k^0_{\rm off}$	free linker detachment rate	10 s^{-1} (26)
δ	linker bond length	1 nm (17)
k	linker stiffness	10^{-4} N/m (text)
ρ_0	density of available linkers	10^{14} m^{-2} (text)
R	cell radius	10 μm (28)
γ	membrane surface tension	5×10^{-5} N/m (11)
κ	membrane bending ridigity	10^{-19} J (30)
γ_m	cortical tension	5×10^{-3} N/m (this work)

where κ is the bending modulus and $\sigma = \rho_{b,\rm eq} k u_{\rm eq}$. As before, the restoring elastic forces exerted by the linkers are treated within a continuous approximation, and membrane fluctuations between bound linkers are not accounted for. This description is appropriate for length scales larger than the average spacing between linkers $\rho_0^{-1/2} \sim 100$ nm.

Membrane deformations induce Stokes flows in the surrounding fluid. These flows mediate long-range hydrodynamic interactions in the membrane, leading to a nonlocal membrane dynamics that is better treated in Fourier space. The full dynamical problem requires a proper treatment of cytosol permeation through the porous cortex and the (less) porous lipid membrane at all length scales (36,37). For simplicity, we restrict ourselves to a simplified treatment, where cytosol permeation through the cortex is only included for the lowest Fourier mode $q = 0$. The other modes are treated below neglecting the effect of the cortex on hydrodynamics, as is appropriate for sufficiently large membrane-cortex distances and/or large cortex mesh size. The effect of finite cortex permeation is studied in Section S4 in the Supporting Material. Using standard results of membrane hydrodynamics (38) together with Eq. 11, the dynamics of long-wavelength membrane deformations read

$$\partial_t \delta\tilde{u}_{\vec{0}} = -\frac{1}{\eta}\left[\rho_{b,\rm eq} k \delta\tilde{u}_{\vec{0}} + \frac{\sigma}{\rho_{b,\rm eq}}\delta\tilde{\rho}_{b,\vec{0}}\right], \tag{12}$$

$$\partial_t \delta\tilde{u}_{\vec{q}} = -\frac{1}{4\eta_c q}\left[\left(\kappa q^4 + \gamma q^2 + \rho_{b,\rm eq} k\right)\delta\tilde{u}_{\vec{q}} + u_{\rm eq} k \delta\tilde{\rho}_{b,\vec{q}}\right], \tag{13}$$

where $\vec{q}$ is the wave-vector. Within our approximation, the relaxation dynamics of the mode $q = 0$ (Eq. 12) is decoupled from the other modes (Eq. 13) at the linear level of perturbations. Equation 12 can be seen as a linearized version of Eq. 2 when transformed back to real space.

In turn, the dynamics of the long-wavelength perturbations of the density of bonds reads

$$\begin{aligned} \partial_t \delta\rho_b(\vec{x}) = &-\frac{k\delta}{k_{\rm B}T} k^0_{\rm off} e^{k u_{\rm eq}\delta/(k_{\rm B}T)} \rho_{b,\rm eq}\delta u(\vec{x}) \\ &- \left[k_{\rm on} + k^0_{\rm off} e^{k u_{\rm eq}\delta/(k_{\rm B}T)}\right]\delta\rho_b(\vec{x}). \end{aligned} \tag{14}$$

Equations 12–14 completely specify the dynamics of linear perturbations around the flat membrane state, both for the membrane displacement u and the density of bonds ρ_b. However, in the limit of long wavelengths, membrane deformations proceed much more slowly than linker kinetics. In general, membrane dynamics is slower than linker kinetics at length scales above a cross-over wavelength $\lambda_{\rm cross}$, which is determined from an analysis of the eigenvalues and eigenvectors of the dynamical system in Eqs. 13 and 14. With the parameters given in Table 1, this cross-over occurs in the bending-dominated regime, for which

$\lambda_{\mathrm{cross}} \simeq 2\pi(\kappa/(4\eta_c k_{\mathrm{on}}))^{1/3} \sim 0.4\ \mu$m. For larger length scales, the kinetics of the linkers shown in Eq. 14 is always essentially equilibrated and an adiabatic approximation may be used. The system can then be described in terms of only the slow variable δu:

$$\partial_t \delta\tilde{u}_{\vec{q}} = -\frac{\kappa q^4 + \gamma q^2 + \rho_{b,\mathrm{eq}} k}{4\eta_c q}\,\delta\tilde{u}_{\vec{q}}. \tag{15}$$

Under the adiabatic approximation, the dispersion relation of membrane dynamics $\omega(q) = -(\kappa q^4 + \gamma q^2 + \rho_{b,\mathrm{eq}}k)/(4\eta_c q)$ features a maximum due to membrane-cortex adhesion (see Section S2.1 in the Supporting Material for details). This maximum naturally defines a correlation length for shape fluctuations, λ_c, below which the membrane can be seen as essentially rigid. This correlation length depends on a combination of both mechanical properties of the membrane and of the linkers:

$$\lambda_c = 2\pi\left[\frac{6\kappa/\gamma}{\left(1 + 12\kappa\rho_{b,\mathrm{eq}}k/\gamma^2\right)^{1/2} - 1}\right]^{1/2}. \tag{16}$$

With the values given in Table 1, we find $\lambda_c \sim 0.6\ \mu$m for an unperturbed cell ($\rho_{b,\mathrm{eq}} \simeq \rho_0$). This value is larger than both the cross-over wavelength of the free membrane undulations, $\lambda = 2\pi\sqrt{\kappa/\gamma} \sim 0.3\ \mu$m, and the spacing between linkers, ${\rho_0}^{-1/2} \sim 0.1\ \mu$m. The computed correlation length is slightly smaller than the pipette radius, so the approximation of a rigid membrane is only marginally valid in that case. However, it becomes more accurate near the unbinding transition because the correlation length λ_c increases with decreasing density of bonds ρ_b (see Section S3 of the Supporting Material for details). In the general case, including all hydrodynamic effects of the cortex, the value of λ_c may differ from Eq. 16 or, for low cortex porosity and short membrane-cortex distances, it may not even be well defined (see Section S4 in the Supporting Material for details).

Finally, at the mean-field level, the critical stress σ^* at which the membrane detaches from the cortex is not affected by membrane undulations because the $q = 0$ mode is the first one to become unstable in the framework of Eqs. 12–14. Fluctuations of the membrane shape may, however, create regions of locally low linker density and high linker stress, thereby widening the unbinding transition boundary.

Fluctuation spectroscopy

The formulation of an adhesion model accounting for membrane undulations provides an appropriate framework to extract additional information about membrane-cortex adhesion from the statistics of membrane fluctuations. For instance, applying the energy equipartition theorem to Eq. 11 one obtains, under the adiabatic approximation, a membrane structure factor of

$$S(q) = \frac{k_{\mathrm{B}}T}{\kappa q^4 + \gamma q^2 + \rho_{b,\mathrm{eq}}k}, \tag{17}$$

where $\rho_{b,\mathrm{eq}}$ is the equilibrium value of the density of bound linkers (see Section S2.2 of the Supporting Material for details). This result is consistent with the situation of a membrane confined in a harmonic potential (39–41). Here, the confinement contribution explicitly arises from the attachment kinetics of the linkers via the adiabatic approximation. This fact allows us to experimentally determine the density of bound linkers, $\rho_{b,\mathrm{eq}}$, from measurements of the static structure factor of the cell membrane (42). Specifically, the long-wavelength limit $q \to 0$ needs to be measured in fluctuation microscopy experiments in order to determine $\rho_{b,\mathrm{eq}}$ from Eq. 17. Transforming Eq. 17 to real space, the mean-square amplitude of membrane undulations reads (see Section S2.3 of the Supporting Material for details):

$$\sqrt{\langle \delta u^2 \rangle} \simeq \sqrt{\frac{k_{\mathrm{B}}T}{8\sqrt{\kappa\rho_{b,\mathrm{eq}}k}}} \sim 4\ \mathrm{nm}. \tag{18}$$

Finally, the model in the previous section also provides dynamical information on membrane undulations. Specifically, the power spectral density of membrane fluctuations can be shown to take the form (43,44)

$$S(\omega) = \frac{4\eta_c k_{\mathrm{B}}T}{\pi}\int_{q_{\min}}^{q_{\max}} \frac{dq}{\left(4\eta_c\omega\right)^2 + \left(\kappa q^3 + \gamma q + \rho_{b,\mathrm{eq}}k/q\right)^2}, \tag{19}$$

where $q_{\min}$ and $q_{\max}$ are the cutoff values of the wave-vector q. In our model, either the perimeter of the cell, the correlation length of cortex undulations, or the radius of the pipette in the experimental setup proposed in Fig. 3 *a* sets the large-wavelength cutoff, $q_{\min} \sim 1/R$, and the short-wavelength cutoff is set by the spacing of the linkers: $q_{\max} = 2\pi/{\rho_0}^{-1/2}$. In fluctuation spectroscopy experiments, the laser focal diameter sets the limitation for the latter (43,44).

Membrane-cortex detachment induced by micropipette aspiration is a rather invasive procedure to assess the stability of the membrane-cortex cellular interface. An alternative approach could be to monitor membrane fluctuations for different aspiration pressures using fluctuation spectroscopy, as sketched in Fig. 3 *a*. Fig. 3 *b* shows the power spectrum density (Eq. 19) in the limit $\gamma \to 0$ both for bending-dominated and adhesion-dominated membrane fluctuations. The high-frequency limits were previously obtained:

$$S(\omega) \approx \frac{k_{\mathrm{B}}T}{6\left(2\kappa\eta_c^2\right)^{1/3}\omega^{5/3}}$$

for $\lambda_c q_{\max} >> 1$, and

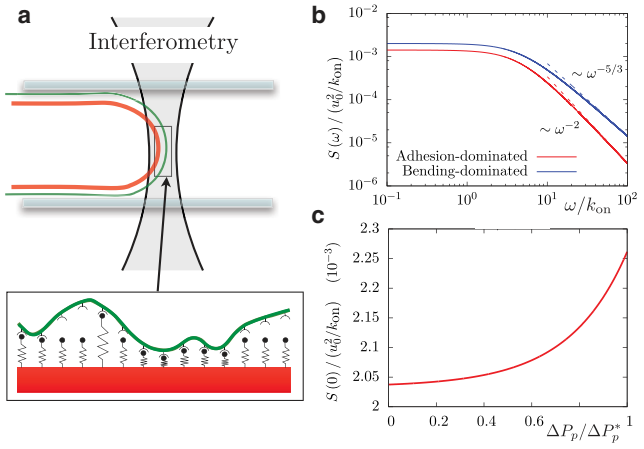

FIGURE 3 Density of membrane-cortex bonds from fluctuation spectroscopy experiments. (*a*) Illustration of a combined spectroscopy and micropipette experiment that could probe the density of membrane-cortex bonds. (*b*) Power spectral density calculated from Eq. 19 in the limit of vanishing surface tension ($\gamma = 0$), both for adhesion-dominated and bending-dominated membrane fluctuations. (*Dashed lines*) Known high-frequency limits. The rescaling length u_0 is defined as $u_0 \equiv k_BT/(k\delta)$. Parameters are taken from Table 1, with $\rho_{b,eq} = \rho_0$, and the power spectrum is integrated from $q_{min} = 1/R$ to $q_{max} = 2\pi/d$, with $d = 0.5\ \mu$m the focal diameter of the optical trap (44). (*c*) Low-frequency plateau of the power spectrum for adhesion-dominated fluctuations (Eq. 21) as a function of the pressure on the membrane. To see this figure in color, go online.

$$S(\omega) \approx \frac{k_BTq_{max}}{4\pi\eta_c\omega^2}$$

otherwise (43–45) (see more details in Section S2.4 of the Supporting Material). However, our model gives an analytical expression for the full power spectrum in the adhesion-dominated regime ($q_{max} < [\rho_{b,eq}k/\kappa]^{1/4}$):

$$\lim_{\kappa,\gamma\to 0} S(\omega) = \frac{k_BT}{4\pi\eta_c\omega^2}\left[q_{max} - q_{min} + \frac{\rho_{b,eq}k}{4\eta_c\omega} \times\left[\arctan\left(\frac{4\eta_c q_{min}\omega}{\rho_{b,eq}k}\right) - \arctan\left(\frac{4\eta_c q_{max}\omega}{\rho_{b,eq}k}\right)\right]\right]. \quad (20)$$

The density of membrane-cortex bonds $\rho_{b,eq}$ can be extracted by fitting this expression to experimental measurements. In particular, if adhesion dominates membrane fluctuations, $\rho_{b,eq}$ can be simply obtained from the plateau of the power spectrum at low frequencies:

$$\lim_{\omega\to 0}\lim_{\kappa,\gamma\to 0} S(\omega) = \frac{4\eta_c k_BT}{3\pi\left(\rho_{b,eq}k\right)^2}\left(q_{max}^3 - q_{min}^3\right). \quad (21)$$

The value of this plateau is plotted in Fig. 3 *c* as a function of the pressure on the membrane, ΔP, which modifies the density of bound linkers. Experimentally, the pressure on the membrane can be varied, either decreasing cortical tension by inhibiting myosin activity or via micropipette suction. Hence, we propose combined spectroscopy and micropipette experiments, as illustrated in Fig. 3 *a*, to test the predictions in Fig. 3 and estimate the density of membrane-cortex bonds. Note that the tip of the aspirated membrane is not flat, but is on average hemispherical with a radius of curvature matching the pipette radius. A rigorous analysis of the fluctuation spectrum should be done using spherical harmonics rather than Fourier transform. Furthermore, Eq. 19 does not account for the hard-wall repulsion introduced by the pipette walls. As discussed in Betz and Sykes (44), this introduces differences in the low frequency limit of the power spectrum. However, this should not affect the pressure dependence of the zero-frequency power spectrum shown in Fig. 3 *c*. The correction to Eq. 20 due to a finite average membrane curvature can be reduced by increasing the radius of the micropipette, or by tuning myosin activity rather than using a micropipette to modify the average density of bond linkers.

The measurement of the density of membrane-cortex linkers from fluctuation spectroscopy is complementary to the quantitative determination of the cortical activity and adhesion energy from micropipette experiments, as discussed above. Indeed, data on fluctuation spectra of generic eukaryotic cells other than red blood cells are still lacking. Peukes and Betz (46) have recently obtained such spectra in blebs during their growth stage, while the cortex is still reforming and, thus, weak. However, information about the full cortex could only be extracted from experiments probing the fluctuations of strongly adhered membranes instead of blebs. Peukes and Betz (46) analyze the fluctuation spectra as that of isolated membranes, with the effect of the cortex only incorporated into an effective tension of the membrane. In contrast, our model accounts for the effect of the adhesion to the cortex via the kinetics of the linkers, thus providing a theoretical framework in which to consistently interpret fluctuation spectroscopy experiments on strongly adhered cell membranes.

As a final comment, it is worth stressing that, in this article, we have only addressed passive fluctuations of thermal origin. In general, different active processes could potentially modify the presented scenario. Typically, active processes are quantitatively most pronounced at low frequencies. At high enough frequencies it has been shown that the role of active fluctuations can be incorporated through an increased effective temperature of the membrane (39,47,48). A detailed analysis of this point is beyond the scope of this work and is deferred to future work.

CONCLUSIONS

We have described a model for membrane-cortex adhesion that relates the unbinding pressure and adhesion energy measured in micropipette experiments to two cellular parameters, the membrane-cortex ligand density and the myosin-driven cortical activity. The validity of the model

is qualitatively discussed, although a complete set of experiments will be required for a complete validation. The proposed relationship between unbinding pressure and cortical activity provides a method to measure the cortical activity by means of micropipette aspiration experiments. Accounting for membrane undulations allows us to relate the fluctuation spectrum of the membrane to the density of bound membrane-cortex bonds, thus providing a method for measuring this quantity in fluctuation spectroscopy experiments. Together, these experiments could give access to quantitative information about membrane-cortex adhesion in the framework of our model.

SUPPORTING MATERIAL

Supporting Materials and Methods, six figures, and one table are available at http://www.biophysj.org/biophysj/supplemental/S0006-3495(15)00226-X.

ACKNOWLEDGMENTS

R.A. acknowledges support from Fundació "la Caixa", J.C. acknowledges financial support of the Ministerio de Economa y Competitividad under projects No. FIS2010-21924-C02-02 and No. FIS2013-41144-P and the Generalitat de Catalunya under projects No. 2009 SGR 14 and No. 2009 SGR 878, and P.S. acknowledges support from the Human Frontier Science Program under grant No. RGP0058/2011.

SUPPORTING CITATIONS

References (49–54) appear in the Supporting Material.

REFERENCES

1. Coleman, M. L., E. A. Sahai, …, M. F. Olson. 2001. Membrane blebbing during apoptosis results from caspase-mediated activation of ROCK I. *Nat. Cell Biol.* 3:339–345.
2. Vermeulen, K., D. R. van Bockstaele, and Z. N. Berneman. 2005. Apoptosis: mechanisms and relevance in cancer. *Ann. Hematol.* 84:627–639.
3. Blaser, H., M. Reichman-Fried, …, E. Raz. 2006. Migration of zebrafish primordial germ cells: a role for myosin contraction and cytoplasmic flow. *Dev. Cell.* 11:613–627.
4. Yoshida, K., and T. Soldati. 2006. Dissection of amoeboid movement into two mechanically distinct modes. *J. Cell Sci.* 119:3833–3844.
5. Fackler, O. T., and R. Grosse. 2008. Cell motility through plasma membrane blebbing. *J. Cell Biol.* 181:879–884.
6. Charras, G., and E. Paluch. 2008. Blebs lead the way: how to migrate without lamellipodia. *Nat. Rev. Mol. Cell Biol.* 9:730–736.
7. Sheetz, M. P. 2001. Cell control by membrane-cytoskeleton adhesion. *Nat. Rev. Mol. Cell Biol.* 2:392–396.
8. Tsujioka, M., S. Yumura, …, S. Yonemura. 2012. Talin couples the actomyosin cortex to the plasma membrane during rear retraction and cytokinesis. *Proc. Natl. Acad. Sci. USA.* 109:12992–12997.
9. Tsukita, S., and S. Yonemura. 1999. Cortical actin organization: lessons from ERM (ezrin/radixin/moesin) proteins. *J. Biol. Chem.* 274:34507–34510.
10. Charras, G. T., M. Coughlin, …, L. Mahadevan. 2008. Life and times of a cellular bleb. *Biophys. J.* 94:1836–1853.
11. Tinevez, J.-Y., U. Schulze, …, E. Paluch. 2009. Role of cortical tension in bleb growth. *Proc. Natl. Acad. Sci. USA.* 106:18581–18586.
12. Rentsch, P. S., and H. Keller. 2000. Suction pressure can induce uncoupling of the plasma membrane from cortical actin. *Eur. J. Cell Biol.* 79:975–981.
13. Seifert, U. 2000. Rupture of multiple parallel molecular bonds under dynamic loading. *Phys. Rev. Lett.* 84:2750–2753.
14. Erdmann, T., and U. S. Schwarz. 2004. Stability of adhesion clusters under constant force. *Phys. Rev. Lett.* 92:108102.
15. Erdmann, T., S. Pierrat, …, U. S. Schwarz. 2008. Dynamic force spectroscopy on multiple bonds: experiments and model. *Europhys. Lett.* 81:48001.
16. Brugués, J., B. Maugis, …, P. Sens. 2010. Dynamical organization of the cytoskeletal cortex probed by micropipette aspiration. *Proc. Natl. Acad. Sci. USA.* 107:15415–15420.
17. Evans, E. 2001. Probing the relation between force—lifetime—and chemistry in single molecular bonds. *Annu. Rev. Biophys. Biomol. Struct.* 30:105–128.
18. Rózycki, B., R. Lipowsky, and T. R. Weikl. 2006. Adhesion of membranes with active stickers. *Phys. Rev. Lett.* 96:048101.
19. Reister-Gottfried, E., K. Sengupta, …, A.-S. Smith. 2008. Dynamics of specific vesicle-substrate adhesion: from local events to global dynamics. *Phys. Rev. Lett.* 101:208103.
20. Krobath, H., B. Różycki, …, T. R. Weikl. 2009. Binding cooperativity of membrane adhesion receptors. *Soft Matter.* 5:3354.
21. Weikl, T. R., M. Asfaw, …, R. Lipowsky. 2009. Adhesion of membranes via receptor-ligand complexes: domain formation, binding cooperativity, and active processes. *Soft Matter.* 5:3213.
22. Reister, E., T. Bihr, …, A.-S. Smith. 2011. Two intertwined facets of adherent membranes: membrane roughness and correlations between ligand-receptors bonds. *New J. Phys.* 13:025003.
23. Hu, J., R. Lipowsky, and T. R. Weikl. 2013. Binding constants of membrane-anchored receptors and ligands depend strongly on the nanoscale roughness of membranes. *Proc. Natl. Acad. Sci. USA.* 110:15283–15288.
24. Bovellan, M., Y. Romeo, …, G. Charras. 2014. Cellular control of cortical actin nucleation. *Curr. Biol.* 24:1628–1635.
25. Kramers, H. 1940. Brownian motion in a field of force and the diffusion model of chemical reactions. *Physica.* 7:284–304.
26. Rognoni, L., J. Stigler, …, M. Rief. 2012. Dynamic force sensing of filamin revealed in single-molecule experiments. *Proc. Natl. Acad. Sci. USA.* 109:19679–19684.
27. Dai, J., H. P. Ting-Beall, …, M. A. Titus. 1999. Myosin I contributes to the generation of resting cortical tension. *Biophys. J.* 77:1168–1176.
28. Merkel, R., R. Simson, …, E. Sackmann. 2000. A micromechanic study of cell polarity and plasma membrane cell body coupling in *Dictyostelium*. *Biophys. J.* 79:707–719.
29. Campillo, C., J. Jerber, …, C. Sykes. 2012. Mechanics of membrane-cytoskeleton attachment in *Paramecium*. *New J. Phys.* 14:125016.
30. Dai, J., and M. P. Sheetz. 1999. Membrane tether formation from blebbing cells. *Biophys. J.* 77:3363–3370.
31. Diz-Muñoz, A., M. Krieg, …, C.-P. Heisenberg. 2010. Control of directed cell migration in vivo by membrane-to-cortex attachment. *PLoS Biol.* 8:e1000544.
32. Borghi, N., and F. Brochard-Wyart. 2007. Tether extrusion from red blood cells: integral proteins unbinding from cytoskeleton. *Biophys. J.* 93:1369–1379.
33. Schumacher, K. R., A. S. Popel, …, A. A. Spector. 2009. Computational analysis of the tether-pulling experiment to probe plasma membrane-cytoskeleton interaction in cells. *Phys. Rev. E Stat. Nonlin. Soft Matter Phys.* 80:041905.
34. Zatulovskiy, E., R. Tyson, …, R. R. Kay. 2014. Bleb-driven chemotaxis of *Dictyostelium* cells. *J. Cell Biol.* 204:1027–1044.
35. Boal, D. 2002. Mechanics of the Cell. Cambridge University Press, Cambridge, UK.

36. Gov, N., A. G. Zilman, and S. Safran. 2004. Hydrodynamics of confined membranes. *Phys. Rev. E Stat. Nonlin. Soft Matter Phys.* 70:011104.

37. Strychalski, W., and R. D. Guy. 2013. A computational model of bleb formation. *Math. Med. Biol.* 30:115–130.

38. Seifert, U. 1997. Configurations of fluid membranes and vesicles. *Adv. Phys.* 46:13–137.

39. Gov, N., A. G. Zilman, and S. Safran. 2003. Cytoskeleton confinement and tension of red blood cell membranes. *Phys. Rev. Lett.* 90:228101.

40. Fournier, J.-B., D. Lacoste, and E. Raphaël. 2004. Fluctuation spectrum of fluid membranes coupled to an elastic meshwork: jump of the effective surface tension at the mesh size. *Phys. Rev. Lett.* 92:018102.

41. Merath, R.-J., and U. Seifert. 2006. Nonmonotonic fluctuation spectra of membranes pinned or tethered discretely to a substrate. *Phys. Rev. E Stat. Nonlin. Soft Matter Phys.* 73:010401.

42. Popescu, G., T. Ikeda, …, M. S. Feld. 2006. Optical measurement of cell membrane tension. *Phys. Rev. Lett.* 97:218101.

43. Betz, T., M. Lenz, …, C. Sykes. 2009. ATP-dependent mechanics of red blood cells. *Proc. Natl. Acad. Sci. USA.* 106:15320–15325.

44. Betz, T., and C. Sykes. 2012. Time resolved membrane fluctuation spectroscopy. *Soft Matter.* 8:5317.

45. Helfer, E., S. Harlepp, …, D. Chatenay. 2001. Viscoelastic properties of actin-coated membranes. *Phys. Rev. E Stat. Nonlin. Soft Matter Phys.* 63:021904.

46. Peukes, J., and T. Betz. 2014. Direct measurement of the cortical tension during the growth of membrane blebs. *Biophys. J.* 107:1810–1820.

47. Manneville, J.-B., P. Bassereau, …, J. Prost. 1999. Activity of transmembrane proteins induces magnification of shape fluctuations of lipid membranes. *Phys. Rev. Lett.* 82:4356–4359.

48. Manneville, J.-B., P. Bassereau, …, J. Prost. 2001. Active membrane fluctuations studied by micropipet aspiration. *Phys. Rev. E Stat. Nonlin. Soft Matter Phys.* 64:021908.

49. Guyon, E., J.-P. Hulin, …, C. D. Mitescu. 2001. Physical Hydrodynamics. Oxford University Press, New York.

50. Lin, L. C., and F. L. Brown. 2005. Dynamic simulations of membranes with cytoskeletal interactions. *Phys. Rev. E Stat. Nonlin. Soft Matter Phys.* 72:011910.

51. de Gennes, P. G., and C. Taupin. 1982. Microemulsions and the flexibility of oil/water interfaces. *J. Phys. Chem.* 86:2294–2304.

52. Gov, N., and S. A. Safran. 2004. Pinning of fluid membranes by periodic harmonic potentials. *Phys. Rev. E Stat. Nonlin. Soft Matter Phys.* 69:011101.

53. Safran, S. A. 1994. Statistical Thermodynamics of Surfaces, Interfaces, and Membranes. Addison-Wesley, Boston, MA.

54. Ranft, J., J. Prost, …, J.-F. Joanny. 2012. Tissue dynamics with permeation. *Eur. Phys. J. E Soft Matter.* 35:46.

Supporting material for "Model for probing membrane-cortex adhesion by micropipette aspiration and fluctuation spectroscopy"

Ricard Alert[1], Jaume Casademunt[1], Jan Brugués*[2], and Pierre Sens◇[3]

[1]Departament d'Estructura i Constituents de la Matèria, Universitat de Barcelona, Avinguda Diagonal 647, 08028 Barcelona, Spain
[2]MPI of Molecular Cell Biology and Genetics, MPI for Physics of Complex Systems, Pfotenhauer Strasse 108, 01307 Dresden, Germany
[3]Laboratoire Gulliver, CNRS-ESPCI, UMR 7083, 10 rue Vauquelin, 75231 Paris Cedex 05, France. Present address: Physico-Chimie Curie, CNRS UMR 168, Institut Curie, 11 rue Pierre et Marie Curie, 75231 Paris Cedex 05, France

Contents

1 Flow dissipation in membrane displacements

In this section, the energy dissipation associated to the flows involved in the displacement of the membrane is estimated. This quantity is given by the fluid mechanics

*brugues@mpi-cbg.de
◇pierre.sens@curie.fr

of a viscous flow (1)

$$\dot{E} = 2\eta_f \int_V \vec{\vec{e}} : \vec{\vec{e}}\, dV; \qquad e_{ij} = \frac{1}{2}\left(\frac{\partial v_i}{\partial r_j} + \frac{\partial v_j}{\partial r_i}\right), \tag{1}$$

where η_f is the viscosity of the fluid flowing with a velocity field $\vec{v}$, and $\vec{\vec{e}}$ is the symmetric part of the strain rate tensor $\vec{\nabla}\vec{v}$.

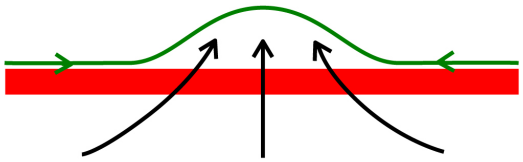

Figure 1: Sketch of membrane (green) and cytosol (black) flows involved in membrane displacements. For instance, during the initial stages of membrane-cortex detachment, i.e. bleb nucleation, the membrane is dragged over the cortex (red) and the cytosol flows through it.

There are two main sources of dissipation associated to membrane displacement, namely the lateral flow of the membrane, and the flow of cytosol through the cortex (Fig. 1). These two contributions are addressed in the two following subsections, respectively. Finally, the cytosol flow is identified as the main source of dissipation in this process. This allows to define an effective viscosity per unit length, η, characterizing the dissipative normal motion of the membrane as in Eq. 1 in the Main Text.

1.1 Membrane flow dissipation

We start by considering the lateral flow of the membrane respect to the underlying cortex. Suppose that the membrane is flowing towards a membrane patch that is inflating. This patch can be thought of as a nucleating bleb of circular projected area of radius a. The increase of the membrane area of this incipient bleb per unit time, $\dot{S}_b$, is given by membrane mass conservation: $\dot{S}_b = 2\pi r\dot{r}$, where r is the distance from any point along the membrane to the center of the bleb (cylindrical coordinates), and $\dot{r}$ is the radial flow speed (Fig. 2).

However, the flowing speed of the membrane must vanish at the points at which it is connected to the cortex through linker molecules. This gives rise to a local velocity gradient of order $\dot{r}/\xi_0 = \dot{S}_b/\left(2\pi r\xi_0\right)$ between any two linkers, with $\rho_0 \equiv \xi_0^{-2}$ the density of linkers. In turn, the global radial velocity gradient of membrane flow is of order $\dot{r}/r = \dot{S}_b/\left(2\pi r^2\right)$. Therefore, the total membrane flow dissipation $\dot{E}_m$ will include the contributions of these two gradients: $\dot{E}_m = \dot{E}_m^{\text{links}} + \dot{E}_m^{\text{global}}$. Then, based on Eq. 1, these are estimated by

$$\dot{E}_m^{\text{links}} \sim 4\pi\eta_m g \int_a^R r dr \left(\frac{\dot{S}_b}{2\pi r\xi_0}\right)^2 = \frac{\eta_m g \dot{S}_b^2}{\pi\xi_0^2} \ln\left(\frac{R}{a}\right) \approx \frac{\eta_m g \dot{S}_b^2}{2\pi\xi_0^2} \ln\left(\frac{S}{4A_b}\right), \tag{2}$$

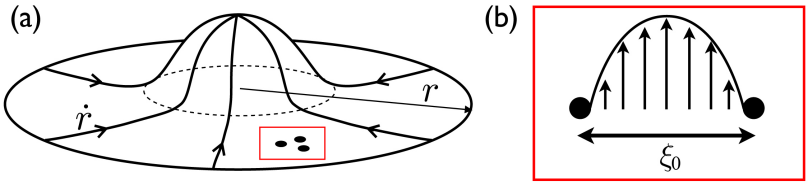

Figure 2: Membrane flow dissipation. (a) Sketch of the membrane flow towards a given patch (dotted line). (b) This flow vanishes at the position of the membrane-cortex linkers (black dots), which results in a gradient of the flow velocity.

$$\dot{E}_m^{\text{global}} \sim 4\pi\eta_m g \int_a^R r dr \left(\frac{\dot{S}_b}{2\pi r^2}\right)^2 \approx \frac{\eta_m g \dot{S}_b^2}{2\pi a^2} = \frac{\eta_m g \dot{S}_b^2}{2A_b}. \tag{3}$$

Here, η_m is the viscosity of the membrane, g its thickness, and R is the cell radius. Accordingly, $S = 4\pi R^2$ is the total visible area of the cell membrane, and $A_b = \pi a^2$ is the projected circular area of the incipient bleb. Our continuum approach describes membrane displacements at length scales larger than ξ_0^2. As a consequence, $A_b > \pi\xi_0^2$ and the local dissipation between linkers, $\dot{E}_m^{\text{links}}$, is expected to dominate membrane flow dissipation.

1.2 Cytosol flow dissipation

Next we compute the energy dissipation rate due to the flow of the cytosol during membrane displacements. In the incompressible regime of cytosol flow, mass conservation reads $\dot{V}_b = 4\pi\varrho^2 v_\varrho$, where V_b is the volume of the incipient bleb, ϱ is now the distance from any point in the cytoplasm to the tip of the bleb (spherical coordinates), and v_ϱ is the fluid velocity at this point. As for the membrane flow, there are two velocity gradients contributing to dissipation; in this case: $\dot{E}_c = \dot{E}_c^{\text{cortex}} + \dot{E}_c^{\text{global}}$. The first one corresponds to the flow of the cytosol through the cortex, which generates velocity gradients of order $v_\varrho/\xi = \dot{V}_b/\left(4\pi\varrho^2\xi\right)$ only inside the cortex. The second one corresponds to the global radial velocity gradient of order $v_\varrho/\varrho = \dot{V}_b/\left(4\pi\varrho^3\right)$ spanning throughout the cytoplasm.

The computation of the cortex term can be done by considering the cortex as a porous material. In this sense, the cortex is viewed as an array of thin capillary tubes of typical radius ξ, so that cylindrical coordinates are the most appropriate in this case. We also consider that the flow of the cytosol through the cortex is along the axial coordinate z and is restricted to the cortical area where the bleb is nucleating (Fig. 1), i.e. a circular area of radius a. Therefore, the number of capillary tubes involved in the cytosol flow through the cortex is $\sim a^2/\xi^2$, so that the total dissipation is this number times the dissipation along one tube. In turn, the cortex is considered to be separated a distance $\sim a$ from the tip of the incipient bleb, so that it is located at $a < z < a + h$, where h is its thickness. Then, using Eq. 1 as before:

$$\dot{E}_c^{\text{cortex}} \sim \frac{a^2}{\xi^2} 4\pi\eta_c \int_a^{a+h} dz \int_0^{\xi} r dr \left(\frac{\dot{V}_b}{4\pi z^2 \xi}\right)^2 \approx \frac{\eta_c h \dot{V}_b^2}{4\pi\xi^2 a^2} = \frac{\eta_c h \dot{V}_b^2}{4\xi^2 A_b}, \tag{4}$$

where we have used $h < a$ to obtain an approximate expression valid for the large length-scale motion that our model describes.

Finally, the global term is dealt with using spherical coordinates in Eq. 1:

$$\dot{E}_c^{\text{global}} \sim 8\pi\eta_c \int_a^R \varrho^2 d\varrho \left(\frac{\dot{V}_b}{4\pi\varrho^3}\right)^2 \approx \frac{\eta_c \dot{V}_b^2}{6\pi a^3} = \frac{\sqrt{\pi}\,\eta_c \dot{V}_b^2}{6A_b^{3/2}}. \tag{5}$$

Similar to the case of the membrane dissipation, since $A_b > \pi\xi^2$, the contribution of the permeation through the cortex is expected to dominate the dissipation associated to cytosol flow.

1.3 Effective viscosity of membrane displacements

In conclusion, an estimate for the rate of energy dissipation due to the flows involved in sufficiently extended membrane displacements is given by

$$\dot{E} \sim \dot{E}_m^{\text{links}} + \dot{E}_c^{\text{cortex}} \sim \frac{\eta_m g \dot{S}_b^2}{2\pi\xi_0^2} \ln\left(\frac{S}{4A_b}\right) + \frac{\eta_c h \dot{V}_b^2}{4\xi^2 A_b}, \tag{6}$$

where only the relevant contributions of the membrane and cytosol flows have been included. Next, $\dot{S}_b$ and $\dot{V}_b$ need to be estimated in terms of membrane displacement u and speed $\dot{u}$. This can be done by considering the shape of the incipient bleb as a spherical cap of radius R_b, polar radius a, and height u. Then,

$$S_b \sim 2\pi R_b u, \qquad V_b \sim \pi R_b u^2; \qquad R_b = \frac{1}{2}\left(\frac{a^2}{u} + u\right). \tag{7}$$

The polar radius a is assumed to remain constant during the inflation of the bleb, while both u and R_b change. Then, the previous expressions need to be rewritten in terms of a single dynamical variable, namely u:

$$S_b \sim \pi\left(a^2 + u^2\right), \qquad V_b \sim \frac{\pi a^2}{2} u \tag{8}$$

to the lowest order in the height u. Now, if the bleb is inflating at a speed $\dot{u}$,

$$\dot{S}_b \sim 2\pi u \dot{u}, \qquad \dot{V}_b \sim \frac{\pi a^2}{2}\dot{u}. \tag{9}$$

According to Eq. 6, this means that the main contribution to dissipation is the flow of cytosol through the cortex for small enough membrane displacements u, to which our linear model is restricted:

$$\dot{E} \sim \frac{\eta_c h A_b}{4\xi^2}\dot{u}^2. \tag{10}$$

This allows to define $\mu_{\text{eff}} \sim \eta_c h A_b/\xi^2$ as the effective drag coefficient for the overdamped motion of the membrane: $F = \mu_{\text{eff}}\dot{u}$. Then, when the dynamics of uniform membrane displacements is specified per unit area, Eq. 1 in the Main Text is retrieved together with the mentioned definition of the effective viscosity per unit length η, given by:

$$\eta \equiv \frac{\mu_{\text{eff}}}{A_b} \sim \eta_c \frac{h}{\xi^2}. \tag{11}$$

It is worth remarking that the overdamped limit for membrane dynamics has been argued to be valid in (2).

2 Membrane undulations

2.1 Adhesion-induced correlations

Under the adiabatic approximation, and at length scales larger than $\rho_0^{-1/2}$, membrane dynamics is fully described in terms of the dispersion relation

$$\omega(q) = -\frac{\kappa q^4 + \gamma q^2 + \rho_{b,\mathrm{eq}} k}{4\eta_c q}, \tag{12}$$

as given by Eq. 15 in the Main Text. Because of membrane-cortex adhesion, the dispersion relation features a maximum at a finite wavelength. Fig. 3 shows that the nonmonotonic behaviour of the dispersion relation is associated to adhesion, disappearing in its absence ($\rho_{b,\mathrm{eq}} = 0$). Indeed, membrane-cortex adhesion is also responsible for the divergence of the dispersion relation at large wavelengths, which disappears if the hydrodynamic effects of the cortex are accounted for (see section 4).

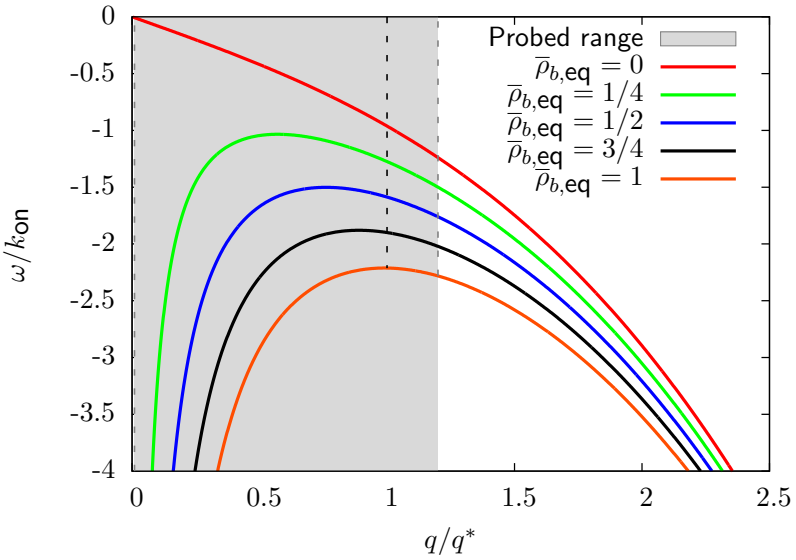

Figure 3: Growth rate of a membrane undulation of wave-vector q for different values of the fraction of bound linkers $\overline{\rho}_{b,\mathrm{eq}} = \rho_{b,\mathrm{eq}}/\rho_0$. The rescaling wave-vector is defined as $q^* = 2\pi/\lambda^*$ with $\lambda^* \equiv \lambda_c(\rho_0)$. The range of wave-vectors experimentally explored in (3) is shaded in grey. This indicates that the non-monotonicity of the dispersion relation due to membrane-cortex adhesion could be probed in fluctuation spectroscopy experiments

The finite wavelength $\lambda_c(\rho_{b,\mathrm{eq}})$ at which the growth rate $\omega(q)$ is maximum, gives the length scale of membrane deformations that feature the slowest relaxation. Consequently, this wavelength acts as a correlation length of membrane undulations.

2.2 Membrane structure factor

Under the adiabatic approximation, and at length scales larger than $\rho_0^{-1/2}$, the structure factor of membrane fluctuations reads

$$S(q) = \frac{k_B T}{\kappa q^4 + \gamma q^2 + \rho_{b,\mathrm{eq}} k}, \tag{13}$$

as given in Eq. 17 of the Main Text. Fig. 4 plots the dependence of the structure factor on the wave-vector q, showing that long-wavelength undulations are the most prominent in terms of amplitude. This fact reinforces the picture of the adhered membrane as a rigid-like object at short scales, with no relevant contribution of undulations. In particular, Fig. 4b shows that fluctuations of length scale smaller than λ^* are not associated to an increase of stress of the linkers, and this should not contribute to setting the location of the unbinding transition. Hence, this explains the role of λ^* as a correlation length separating the rigid-like and undulated regimes of the membrane.

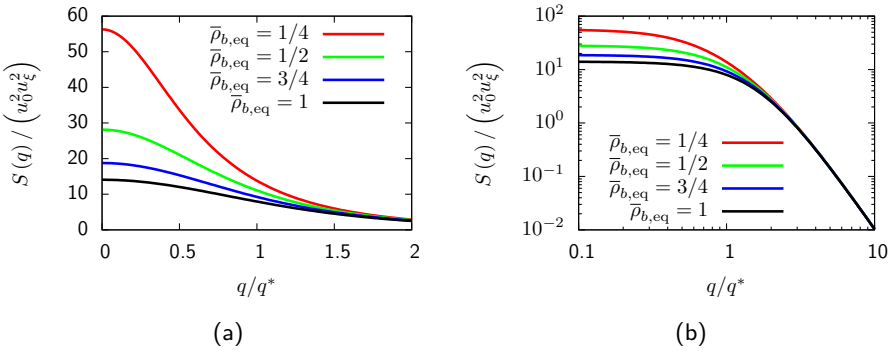

Figure 4: Membrane structure factor as a function of the wave-vector for different values of the fraction of bound linkers $\overline{\rho}_{b,\mathrm{eq}} = \rho_{b,\mathrm{eq}}/\rho_0$. The rescaling lengths are $u_0 \equiv k_B T/(k\delta)$ and $u_\xi \equiv k_B T/(k\xi)$. (a) In linear scale. (b) In logarithmic scale, which evidences the crossover between the regime where adhesion dominates ($\lambda^* q < 1$), and the regime where membrane mechanics dominates ($\lambda^* q > 1$).

2.3 Amplitude of membrane undulations

The mean-square amplitude of membrane undulations can be obtained by Fourier-transforming the membrane structure factor Eq. 13 back to real space:

$$\left\langle \delta u^2(\vec{x}) \right\rangle = \frac{k_B T}{2\pi} \frac{1}{\sqrt{4\kappa\rho_{b,\mathrm{eq}} k - \gamma^2}} \left[\arctan\left(\frac{2\pi^2 \kappa \rho_0 + \gamma}{\sqrt{4\kappa\rho_{b,\mathrm{eq}} k - \gamma^2}} \right) - \arctan\left(\frac{2\kappa (\pi/L)^2 + \gamma}{\sqrt{4\kappa\rho_{b,\mathrm{eq}} k - \gamma^2}} \right) \right]. \tag{14}$$

This is the result for the case $\gamma^2 < 4\kappa\rho_{b,\mathrm{eq}} k$, which is the actual situation for our choice of $k \sim 10^{-4}$ N/m. Next, some limits of Eq. 14 are studied:

- Strong adhesion:

$$\lim_{\rho_{b,\mathrm{eq}}k\to\infty}\left\langle \delta u^2\left(\vec{x}\right)\right\rangle \approx \frac{k_BT\pi\rho_0}{4\rho_{b,\mathrm{eq}}k}, \tag{15}$$

  which does not diverge for large membranes due to adhesion. It corresponds to a rigid and unstretchable membrane fluctuating under the harmonic confinement of the average adhesion potential $\rho_{b,\mathrm{eq}}k$ acting down to the cutoff length $\rho_0^{-1/2}$.

- Low tension:

$$\lim_{\gamma\to 0}\left\langle \delta u^2\left(\vec{x}\right)\right\rangle \approx \frac{k_BT}{8\sqrt{\kappa\rho_{b,\mathrm{eq}}k}}, \tag{16}$$

  which does not diverge either. This situation corresponds, for instance, to the case of a somehow constrained vesicle, where membrane surface tension is negligible as compared to bending rigidity. A constraining harmonic confinement, which can stem from other membranes in a stack (4), the presence of a nearby wall (5), or sparse harmonic attachments (6), produces the same effect as the adhesion term within the adiabatic approximation framework of our model.

- High bending rigidity:

$$\lim_{\kappa\to\infty}\left\langle \delta u^2\left(\vec{x}\right)\right\rangle \approx \frac{k_BTL^2}{4\pi^3\kappa}. \tag{17}$$

  In this case, the root mean-square amplitude diverges linearly with the membrane linear size. This limit corresponds to a free vesicle in the absence of any adhesion or confinement, so that undulations are driven solely by bending rigidity (7).

It is worth exploring the other possible case, namely $\gamma^2 > 4\kappa\rho_{b,\mathrm{eq}}k$, since it could be relevant for some cell types, for instance, presenting a more diluted cortex or softer linkers. In this case, the mean-square amplitude of membrane undulations reads

$$\left\langle \delta u^2\left(\vec{x}\right)\right\rangle = \frac{k_BT}{4\pi}\frac{1}{\sqrt{\gamma^2-4\kappa\rho_{b,\mathrm{eq}}k}}\left[\ln\left(\frac{2\pi^2\kappa\rho_0+\gamma-\sqrt{\gamma^2-4\kappa\rho_{b,\mathrm{eq}}k}}{2\pi^2\kappa\rho_0+\gamma+\sqrt{\gamma^2-4\kappa\rho_{b,\mathrm{eq}}k}}\right)-\right.$$
$$\left.\ln\left(\frac{2\kappa\left(\pi/L\right)^2+\gamma-\sqrt{\gamma^2-4\kappa\rho_{b,\mathrm{eq}}k}}{2\kappa\left(\pi/L\right)^2+\gamma+\sqrt{\gamma^2-4\kappa\rho_{b,\mathrm{eq}}k}}\right)\right]. \tag{18}$$

The limits for this situation are discussed below:

- Weak adhesion:

$$\lim_{\rho_{b,\mathrm{eq}}k\to 0}\left\langle \delta u^2\left(\vec{x}\right)\right\rangle \approx \frac{k_BT}{2\pi\gamma}\ln\left(\frac{L}{\pi}\sqrt{\frac{\gamma}{\kappa}}\right), \tag{19}$$

  which diverges logarithmically for large membranes. This corresponds to the case of a free membrane with contributions both of bending and surface tension to undulations.

- High tension:

$$\lim_{\gamma\to\infty}\left\langle \delta u^2\left(\vec{x}\right)\right\rangle \approx \frac{k_B T}{2\pi\gamma}\ln\left(\rho_0^{1/2}L\right), \tag{20}$$

which also diverges logarithmically for large membranes. This is the result obtained in the absece of adhesion for tension-dominated membrane dynamics (8). This situation might correspond to a strongly stretched membrane due to cortical pulling.

- Low bending rigidity:

$$\lim_{\kappa\to 0}\left\langle \delta u^2\left(\vec{x}\right)\right\rangle \approx \frac{k_B T}{4\pi\gamma}\ln\left(1+\frac{\pi^2\gamma\rho_0}{\rho_{b,\mathsf{eq}}k}\right), \tag{21}$$

which does not diverge for large membranes due to adhesion. This situation corresponds to a very flexible membrane yet under tension, and adherent.

$\gamma^2 < 4\kappa\rho_{b,\mathsf{eq}}k$	no limit	~ 3 nm
	$\rho_{b,\mathsf{eq}}k \to \infty$	~ 6 nm
	$\gamma \to 0$	~ 4 nm
	$\kappa \to \infty$	~ 1 μm
$\gamma^2 > 4\kappa\rho_{b,\mathsf{eq}}k$	no limit	—
	$\rho_{b,\mathsf{eq}}k \to 0$	~ 9 nm
	$\gamma \to \infty$	~ 9 nm
	$\kappa \to 0$	~ 3 nm

Table 1: Numerical estimates for the root mean-square amplitude of membrane undulations $\left\langle \delta u^2\left(\vec{x}\right)\right\rangle^{1/2}$ in different situations and limits. In all cases, the same numerical values of the parameters have been used.

Table 1 summarizes the numerical values of the root mean-square amplitude of membrane undulations for all the cases and limits discussed above. The value $\left\langle \delta u^2\left(\vec{x}\right)\right\rangle^{1/2} \sim 3$ nm corresponding to our case justifies the approximation of considering the membrane-cortex linker molecules as hookean springs, i.e. in their linear elasticity regime.

2.4 Membrane power spectrum

Within the adiabatic approximation, the power spectrum reads

$$S\left(\omega\right) = \frac{4\eta_c k_B T}{\pi}\int_{q_{\mathsf{min}}}^{q_{\mathsf{max}}} \frac{dq}{\left(4\eta_c\omega\right)^2 + \left(\kappa q^3 + \gamma q + \rho_{b,\mathsf{eq}}k/q\right)^2}, \tag{22}$$

as given by Eq. 19 in the Main Text. This expression can not be analytically integrated in general. Next we consider some asymptotic behaviours of this expression. Integration limits are extended to $q_{\mathsf{min}} \to 0$ and $q_{\mathsf{max}} \to \infty$ whenever possible:

- No adhesion. Tension-dominated regime, low frequencies: Low-frequency responses of a non-adhered membrane are found at long wavelengths, and are thus dominated by surface tension: $\lim_{q\to 0}\omega\left(q\right) = \gamma q/\left(4\eta_c\right)$. Therefore,

the low-frequency limit of the power spectrum of a free membrane can be retrieved by imposing a vanishing bending rigidity $\kappa \to 0$:

$$\lim_{\kappa \to 0} S(\omega) = \frac{k_B T}{2\gamma\omega}. \tag{23}$$

- No adhesion. Bending-dominated regime, high frequencies: High relaxation rates of the free membrane occur at $q \to \infty$, implying that they are dominated by the bending rigidity: $\lim_{q\to\infty} \omega(q) = \kappa q^3/(4\eta_c)$. Consequently, the high-frequency limit of the power spectrum of a non-adhered membrane is retrieved by neglecting surface tension $\gamma \to 0$:

$$\lim_{\gamma \to 0} S(\omega) = \frac{k_B T}{6\left(2\kappa\eta_c^2\right)^{1/3}\omega^{5/3}}. \tag{24}$$

- Adhesion-dominated regime, intermediate-high frequencies: As opposed to the behaviour of free membranes, the dispersion relation of a membrane adhered to the cortex in the adiabatic approximation is non-monotonic. Therefore, the relationship between frequencies and wave-vectors is not straightforward. For the range of wave-vectors experimentally explored in (3), with $d_f = 0.5$ μm, we have $\omega(q_{\mathsf{min}}) \gg \omega(q_{\mathsf{max}})$, as shown in Fig. 3. Consequently, the adhesion-dominated regime at long wavelengths corresponds to high frequencies. Using smaller focal light spots could shift the adhesion-dominated regime towards lower frequencies. An analytical expression for the power spectrum in this limit is worked out by setting $\kappa, \gamma \to 0$:

$$\lim_{\kappa,\gamma \to 0} S(\omega) = \frac{k_B T}{4\pi\eta_c\omega^2}\left[q_{\mathsf{max}} - q_{\mathsf{min}} + \right.$$
$$\left. + \frac{\rho_{b,\mathsf{eq}} k}{4\eta_c\omega}\left[\arctan\left(\frac{4\eta_c q_{\mathsf{min}}\omega}{\rho_{b,\mathsf{eq}} k}\right) - \arctan\left(\frac{4\eta_c q_{\mathsf{max}}\omega}{\rho_{b,\mathsf{eq}} k}\right)\right]\right]. \tag{25}$$

- Brownian motion regime, highest frequencies: Finally, at sufficiently high frequencies the power spectrum is only revealing the Brownian motion of the membrane within the cytosol, which only depends on the viscosity of the latter. This limit is thus insensitive to any membrane properties:

$$\lim_{\omega \to \infty} S(\omega) = \frac{k_B T\left(q_{\mathsf{max}} - q_{\mathsf{min}}\right)}{4\pi\eta_c\omega^2}. \tag{26}$$

On the one hand, the first two limits correspond to a non-adhered membrane, for which our model retrieves the predicted (9) and observed (3, 9, 10) scalings $\sim \omega^{-1}$ and $\sim \omega^{-5/3}$ of the power spectrum. These studies also predicted and observed the high-frequency $\sim \omega^{-2}$ behaviour corresponding to the Brownian motion of the membrane within the surrounding fluid. Finally, if the effect of the hydrodynamic confinement due to the presence of the cortex is important, which turns out to be the case for red blood cells, one should expect an intermediate regime scaling as $\sim \omega^{-4/3}$ (11).

3 Validity of the flat-membrane model

Here we analyze the validity of the flat-membrane model as a function of membrane-cortex adhesion. On the one hand, Fig. 5a plots the dependence of the correlation length λ_c on the density of bonds (Eq. 16 of the Main Text), evindencing the increased membrane correlations near the unbinding transition. As a consequence, the simple flat-membrane model becomes more accurate near detachment. On the other hand, Fig. 5b shows the increase in the amplitud of membrane fluctuations (Eq. 14) when membrane-cortex adhesion is weakened, specially at long-wavelength (see also Fig. 4). The magnification of membrane undulations near the unbinding transition implies that a stochastic version of the adhesion models presented in this article may be needed for an accurate study of membrane-cortex detachment.

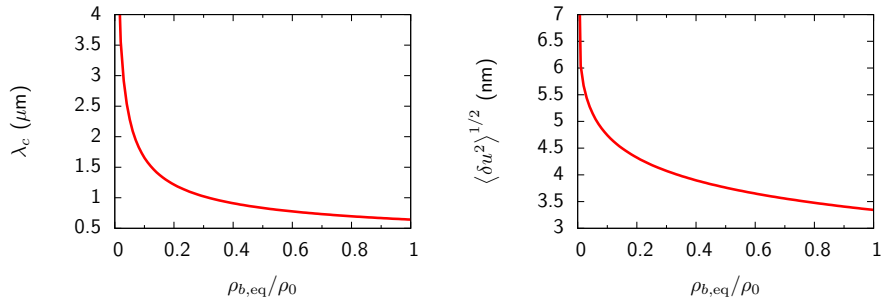

(a) (b)

Figure 5: Membrane correlations and undulations as a function of adhesion. (a) Correlation length of membrane undulations as a function of the equilibrium density of bonds. (b) Root mean-square amplitude of membrane undulations as a function of the equilibrium density of bonds.

4 Influence of a nearby porous cortex on membrane dynamics

Here we comment on the effects of the cortex over the hydrodynamics of the membrane. Under the adiabatic approximation, membrane-cortex adhesion acts as an effective harmonic confining potential of stiffness $\rho_{b,\mathrm{eq}}k$. For a harmonically confined membrane, the presence of a nearby porous wall has been shown to modify the dispersion relation by a mode-dependent factor (5):

$$\omega\left(q\right)=\omega_0\left(q\right)e^{-2Dq}\frac{e^{2Dq}\left(1+4L_pq\right)-1-2Dq-2\left(Dq\right)^2\left(1+2L_pq\right)}{1+4L_pq}, \quad (27)$$

where D is the distance between the membrane and the cortex, and L_p is the cortical permeation length. The latter is defined as $L_p=\sqrt{\eta_c\left(1-\phi_v\right)K_p}$, where η_c is the viscosity of the cytosol, ϕ_v is the volume fraction of the cortex, and K_p is its volume permeability (12). Finally, $\omega_0\left(q\right)$ is the dispersion relation in the absence

of hydrodynamic effects due to the cortex:

$$\omega_0(q) = -\frac{\kappa q^4 + \gamma q^2 + \rho_{b,\mathrm{eq}} k}{4\eta_c q}. \tag{28}$$

Fig. 6 plots the modified relaxation rates for different values of the membrane-cortex distance D and the cortical permeation length L_p. The inclusion of the cortex in the hydrodynamics introduces a cutoff of the relaxation rate at low wave-vectors, in contrast to the divergence shown in Fig. 3. This is the only qualitative change on the dispersion relation arising from the influence of the cortex when it is either far from the membrane or porous enough. In this case, $\omega(q)$ still displays a (possibly local) minimum defining a correlation length. The position of this minimum is slightly shifted, now appearing at longer wavelengths, so that the correlation length of membrane undulations increases from $\lambda^* \sim 0.6$ μm. This would reinforce the adiabatic approximation as well as widen the range of validity of the simple flat-membrane model.

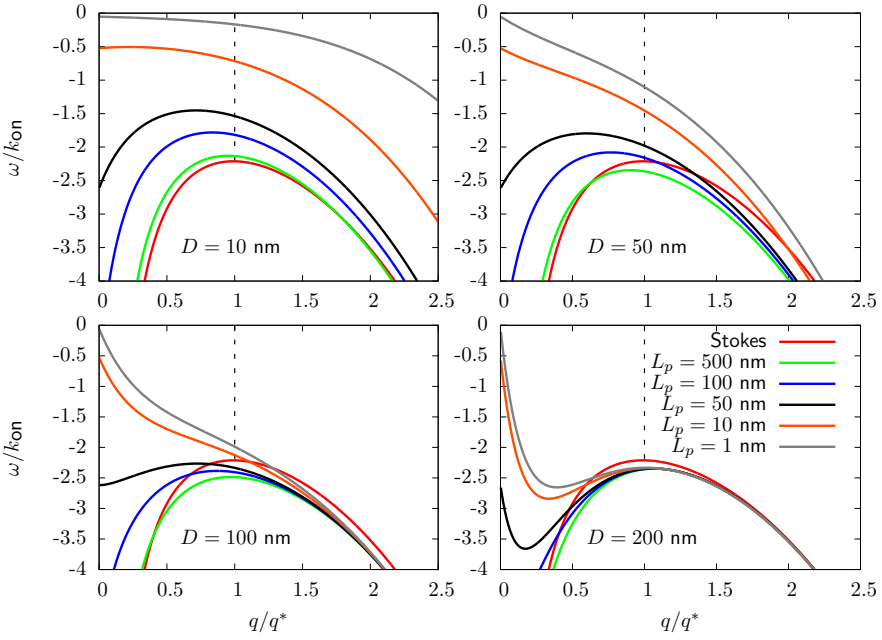

Figure 6: Growth rate of a membrane undulation of wave-vector q for $\rho_{b,\mathrm{eq}} = 1$ and for different values of the membrane-cortex distance D and cortical permeation length L_p. The curve in the absence of cortical influence on membrane hydrodynamics (Stokes) is always shown for comparison.

In turn, low membrane-cortex distances or less permeable cortices would have a stronger influence on membrane hydrodynamics and produce deeper modifications of the dispersion relation. In some cases, the dispersion relation would not even have a local minimum and, therefore, no finite correlation length could be defined. However, this would not invalidate the main conclusions drawn from the analysis of membrane undulations, namely the fact that the flat-membrane model is restricted

to short length scales for large-amplitude undulations, and the possibility to extract the density of bound linkers from fluctuation spectroscopy experiments. Concerning the first one, the lack of a correlation length would simply imply that the crossover length scale below which the flat-membrane model applies could not be estimated a priori. For the second conclusion, the density of bound linkers $\rho_{b,\mathrm{eq}}$ would still be obtainable from the experimental structure factor $S(q)$ or power spectrum $S(\omega)$ but the theoretical fitting curves would not be given by Eq. 13, and Eq. 25, respectively, anymore and they would demand knowledge of D and L_p, instead.

References

1. Guyon, E., J.-P. Hulin, L. Petit, and C. D. Mitescu. 2001. Physical hydrodynamics. Oxford University Press.

2. Lin, L. and F. Brown. 2005. Dynamic simulations of membranes with cytoskeletal interactions. *Phys. Rev. E.* 72:011910.

3. Betz, T. and C. Sykes. 2012. Time resolved membrane fluctuation spectroscopy. *Soft Matter* 8:5317.

4. de Gennes, P. G. and C. Taupin. 1982. Microemulsions and the flexibility of oil/water interfaces. *J. Phys. Chem.* 86:2294–2304.

5. Gov, N., , A. Zilman, and S. Safran. 2004. Hydrodynamics of confined membranes. *Phys. Rev. E.* 70:011104.

6. Gov, N. and S. Safran. 2004. Pinning of fluid membranes by periodic harmonic potentials. *Phys. Rev. E.* 69:011101.

7. Boal, D. 2002. Mechanics of the cell. Cambridge University Press.

8. Safran, S. A. 1994. Statistical thermodynamics of surfaces, interfaces, and membranes. Addison-Wesley.

9. Helfer, E., S. Harlepp, L. Bourdieu, J. Robert, F. MacKintosh, and D. Chatenay. 2001. Viscoelastic properties of actin-coated membranes. *Phys. Rev. E.* 63:021904.

10. Betz, T., M. Lenz, J.-F. Joanny, and C. Sykes. 2009. ATP-dependent mechanics of red blood cells. *Proc. Natl. Acad. Sci. USA.* 106:15320–5.

11. Gov, N. S., A. G. Zilman, and S. A. Safran. 2003. Cytoskeleton confinement and tension of red blood cell membranes. *Phys. Rev. Lett.* 90:228101.

12. Ranft, J., J. Prost, F. Jülicher, and J.-F. Joanny. 2012. Tissue dynamics with permeation. *Eur. Phys. J. E.* 35:46.